Regular Article

Regular and chaotic vibration in a piezoelectric energy harvester with fractional damping

Junyi Cao[1], Arkadiusz Syta[2], Grzegorz Litak[2,3,a], Shengxi Zhou[1], Daniel J. Inman[4], and Yangquan Chen[5]

[1] State Key Laboratory for Manufacturing Systems Engineering, Xi'an Jiaotong University, Xi'an 710049, China
[2] Faculty of Mechanical Engineering, Lublin University of Technology, Nadbystrzycka 36, Lublin 20-618, Poland
[3] Laboratoire de Génie Electrique et Ferroélectricité, Institut National des Sciences Appliquées de Lyon, 69621 Villeurbanne cedex, France
[4] Department of Aerospace Engineering, University of Michigan, Ann Arbor, MI 48109-2140, USA
[5] School of Engineering, University of California, Merced, 5200 North Lake Rd., Merced, CA 95343, USA

Abstract. We examine a vibrational energy harvester consisting of a mechanical resonator with a fractional damping and electrical circuit coupled by a piezoelectric converter. By comparing the bifurcation diagrams and the power output we show that the fractional order of damping changes the system response considerably and affects the power output. Various dynamic responses of the energy harvester are examined using phase trajectory, Fourier spectrum, Multi-scale entropy and 0-1 test. The numerical analysis shows that the fractionally damped energy harvesting system exhibits chaos, and periodic motion, as the fractional order changes. The observed bifurcations strongly influence the power output.

1 Introduction

A recent concept of frequency broadband energy harvesting systems consists of using nonlinear phenomena (such as material nonlinearities), geometrical nonlinearities, and multi-scale responses resulting in the appearance of multiple solutions. The broadband effects can be observed from the nonlinear time series analysis of simulated mathematical models or from measured system responses in experiments. It is well known that the efficiency of many engineered systems may be enhanced by operation in a nonlinear regime. Nonlinear vibrational energy harvesting shows an advantage when the ambient vibration source of energy is variable in amplitude and frequency.

Energy harvesters using the nonlinear effects have been proposed in different configurations [1–7]. Among them an application of a double well potential was proposed [8–13]. Gammaitoni *et al.* [9] and Masana and Daqaq [14] discussed the conditions of inter-well hopping. In fact, the Duffing oscillator, as the simplest model, was used for many energy harvesting simulations, with the addition of electromechanical coupling for the harvesting circuit [15–19]. McInnes *et al.* [20], Kwuimy *et al.* [21] and Martens *et al.* [22] investigated the stochastic resonance phenomena for a nonlinear system with a double potential well.

Recently, in the context of broadband energy harvesting, bifurcations and chaotic vibrations have been studied in several papers. Cao *et al.* [23] and Kwuimy *et al.* [24] studied chaos in the fractionally damped broadband piezoelectric energy generator in the system with additional magnets. Syta *et al.* [25] analysed the dynamic response of a piezoelectric material attached to a bistable laminate plate is examined based on the experimental generated voltage time series. It is worth noting that chaotic vibrations are, in most cases, characterized by moderate amplitude of vibrations and simultaneously give a continuous frequency spectrum, which can be useful for increasing mechanical resonator durability.

In this article we discuss different solutions appearing in the double well system in the presence of the visco-elastic damping with a fractional characteristics. A fractional derivative present in the dynamical systems is usually related to complex phenomena possessing multiple relaxation rates, which is one way to model hysteresis. Especially, we focus on the influence of the fractional order of mechanical damping on the energy harvester dynamical response in terms

---

[a] e-mail: g.litak@pollub.pl

of the voltage output. Occurrence of intra- and inter-well oscillations as well as periodic and chaotic vibrations lead to different efficiencies in energy harvesting. Therefore, we identify the types and characteristic properties of given solutions by using nonlinear methods.

2 Mathematical model and equations of motion

In the present model we considered the vertical flexible beam with fractional damping (fig. 2) and nonharmonic potential dependent on the magnets orientation angle. The differential equations reads:

$$M\ddot{x}(t) + CD^{\alpha}x(t) + Kx(t) - F_m - \Theta u(t) = F_e \tag{1}$$

$$C_p\dot{u}(t) + \Theta\dot{x}(t) + R^{-1}u(t) = 0, \tag{2}$$

where $x(t)$ is the horizontal displacement of the tip mas (magnet) on the beam, M and K are the effective mas and stiffness, C is the fractional damping coefficient with the fractional derivative D^{α} of the damping order α, $u(t)$ is the output voltage, C_p is the capacity of the piezoelectric electrodes, R is electrical resistance and Θ is coupling between mechanical and electrical subsystems. $\dot{y}$ denotes the time derivative of variable y. F_m is the magnetic force inducing nonlinearities in the system, while F_e excitation harmonic force $F_e/M = A\sin(2\pi ft)$. The system parameters have been identified from the experiments: $M = 0.0061\,\text{kg}$; $C = 0.0247\,\text{Ns/m}$; $K = 63.8\,\text{N/m}$; $\Theta = 9.19 \times 10^{-5}\,\text{N/V}$, $R = 10\,\text{M}\Omega$ (parameters after [23]).

In the simulations we change α for the fixed excitation amplitude $A = 0.56\,\text{g}$, where g is the gravitational acceleration, while the frequency was $f = 10\,\text{Hz}$. The nonlinear magnetic force is expanded as a polynomial:

$$-F_m = a_0 + a_1 z(t) + a_2 z^2(t) + \ldots + a_n z^n(t), \tag{3}$$

where $a_0 = 0$, $a_1 = 79.17\,[\text{N/m}]$; $a_2 = 0$; $a_3 = -2.61 \times 10^5\,[\text{N/m}^3]$ and a_n is zero for $n > 3$.

In order to implement the fractional-order operator D^{α} into numerical simulations we used a polynomial expansion. Namely, for the fractional derivative approximation D^{α} we used a continued fraction expansion based on Tustin and/or Euler transformation [26–29].

The continued fraction expansion (CFE) based on the Tustin transformation is

$$Z\{D^{\alpha}\}x(t) = \text{CFE}\left\{\left(\frac{2}{T}\frac{1-z^{-1}}{1+z^{-1}}\right)^{\alpha}\right\}X(z) \approx \left(\frac{2}{T}\right)^{\alpha}\frac{F_p(z^{-1})}{Q_q(z^{-1})}X(z), \tag{4}$$

while CFE based on the Euler transformation is

$$Z\{D^{\alpha}\}x(t) = \text{CFE}\left\{\left(\frac{1-z^{-1}}{T}\right)^{\alpha}\right\}X(z) \approx \left(\frac{1}{T}\right)^{\alpha}\frac{F_p(z^{-1})}{Q_q(z^{-1})}X(z), \tag{5}$$

where $Z\{\cdot\}$ is the Z-transform operator, $X(z)$ represents the Z-transform of $x(t)$,

$$X(z) = Z\{x[n]\} = \sum_n x[n]z^{-n} \tag{6}$$

and T is the sampling period, and n is the discrete time index.

In the numerical simulation, the orders of p and q (in P_p and Q_q polynomials) were equal to 10 and the sampling period T was set to 0.002.

After the CFE decomposition the algebraic expression (eqs. (4) or (5)) can be transformed back to the time domain using the infinite impulse response (IIR) filter approximated to different fractional operators.

3 Numerical simulations and results

Following [23] we use the same set of system parameters. The beam-magnet (fig. 1(a)) system is excited at the base with harmonic excitation. Figure 1(b) shows the restoring force potential $V(x)$ ($F_m - Kx = -\text{d}V(x)/\text{d}x$) used in the calculations.

The simulations were performed for eqs. (1) and (2) using various values of fractional order $\alpha \in (0, 1.5]$. The results for displacement are summarized in figs. 2(a) and (b). The initial conditions were set for $\alpha = 0.01$ as $(x, \dot{x}, u, \dot{u}) = (0, 0, 0, 0)$, and increased by 0.01 quasistaticaly during the simulations.

Figures 2(a) and (b) show the bifurcation diagram of displacement using the distribution local maxima $x_{\max}$ and the main value of displacement $\bar{x}$ calculated for 51 cycles, respectively. Note that the single or multiple discrete lines
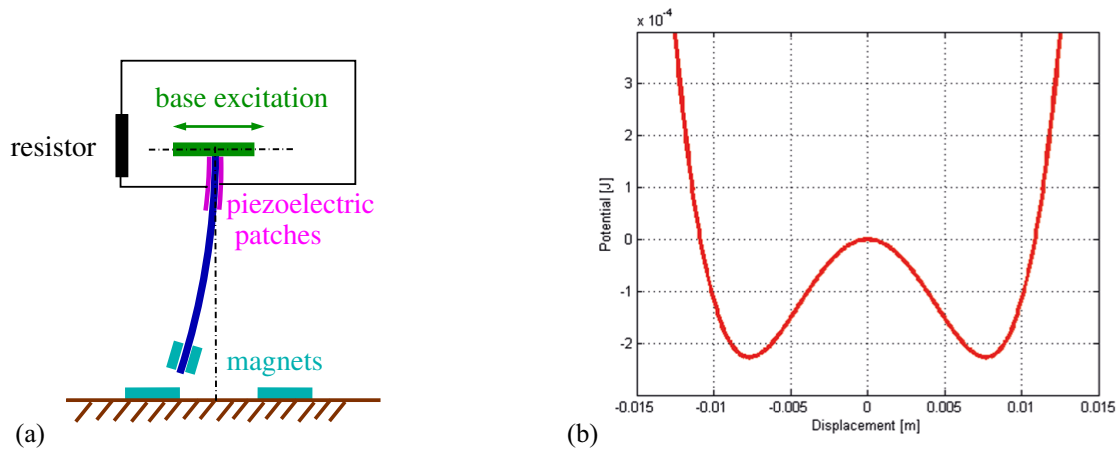
Fig. 1. (a) Schematic of the nonlinear energy harvester with a flexible beam, piezoelectric layer, and external magnets. (b) Potential including magnetic and elastic components. Note the position of the potential minima are $x_{1/2} = \mp 0.0077\,\text{m}$.
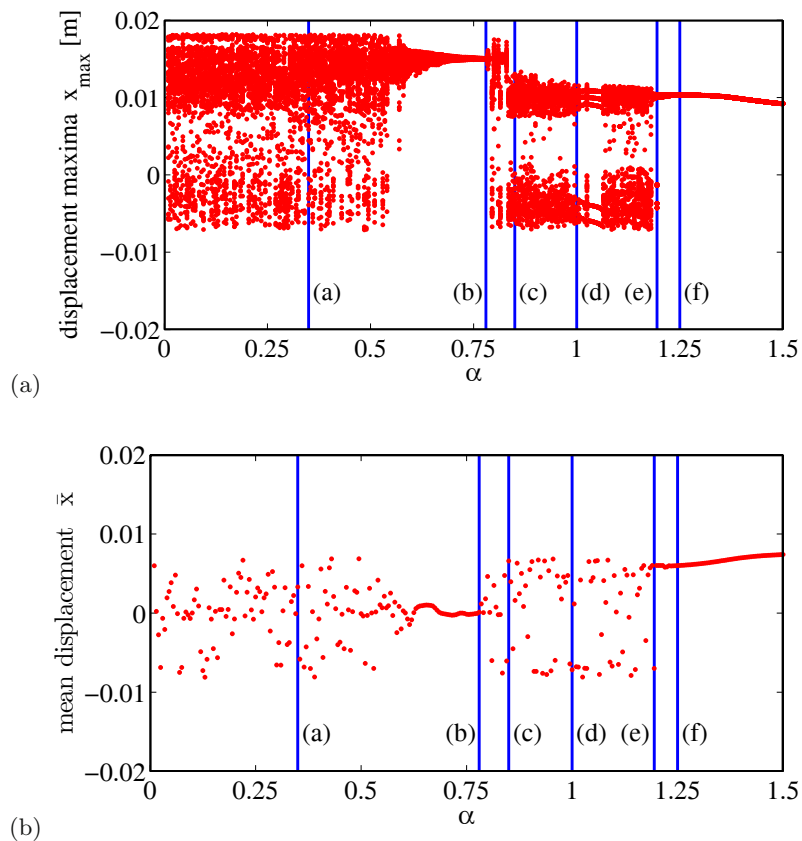

Fig. 2. (a) Bifurcation diagrams of displacement local maxima *versus* the fractional order α; (b) the mean value $\bar{x}$ *versus* the fractional order α.

($\alpha \in [0.53, 0.78]$, $[1.00, 1.50]$ with small windows in $[0.79, 0.99]$), in fig. 2(a), correspond to the one or multiperiod regular solutions while some wider distributions of maxima ($\alpha \in (0, 0.52]$, and $[0.79, 0.99]$ excluding some small regular windows inside) indicate the nonperiodic behaviour. On the other hand, the $\bar{x}$ shows the evolution of the center of oscillations. It is easy to notice that for $\alpha < 1$ the center of oscillation is a more symmetric distribution (note that for nonperiodic solution the mean value of $\bar{x}$ would tend to 0 asymptotically) and for $\alpha > 1$ the center of oscillation is clearly shifted to one of potential minima with $x \approx 0.008$. Interestingly, for larger α we have a stronger damping effect and the system response stays in one of the potential wells close to its minimum (see x_2 in fig. 1(b)).

In fig. 3(a) we show the bifurcation diagram using the voltage maxima. The diagram shows the changes in periodicity response corresponding to fig. 2(a). There are three main regions of the discrete points aggregations representing various
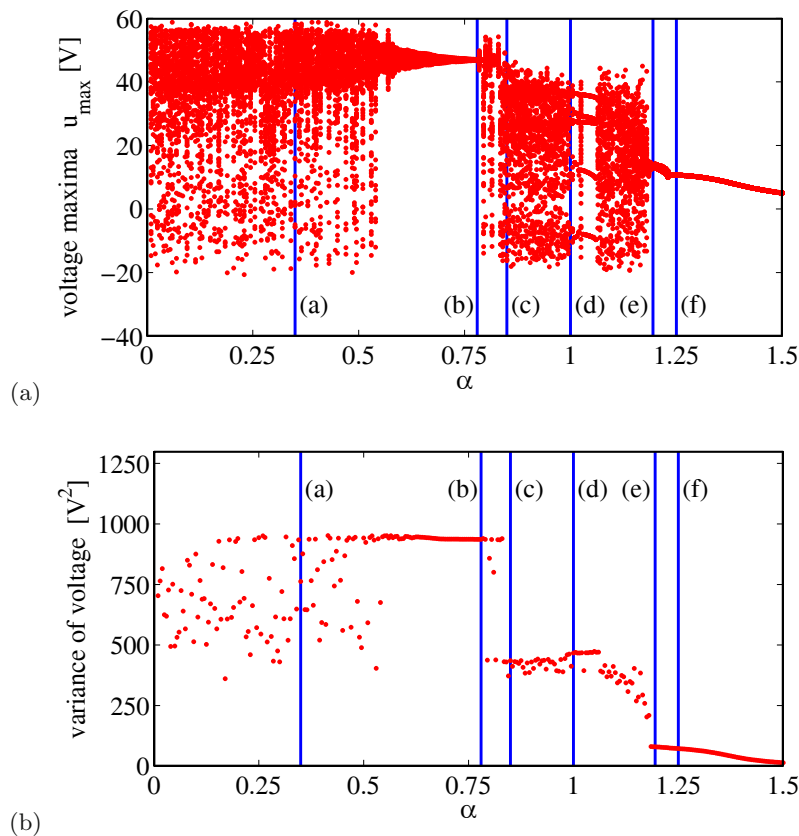
Fig. 3. (a) Bifurcation diagrams of displacement local voltage output *versus* the fractional order α; (b) Variance voltage, Var(u), output against α.

types of periodic responses (depending on the number of discrete points) and more homogeneous broad distributions representing a nonperiodic response. More importantly the different solutions relate to different power outputs. This value was represented by the variance of the voltage and plotted in fig. 3(b). Note that the occurance of periodic solutions with larger amplitude is the most effective for energy harvesting. The noperiodic (chaotic) solutions are showing variable power. Finally, for larger α we reach the region of single well vibrations of the beam with small variation of voltage and consequently decreased power output. In summary, by increasing α the power output increases initially to reach the maximum value for large amplitude periodic oscillations, however further increasing α decreases the power as the rate of mechanical damping losses are larger.

Corresponding to the dynamics represented in figs. 2 and 3, the system response is changing considerably. Next we present the corresponding time series related to $\alpha = 0.35, 0.78, 0.85, 1.00, 1.195, 1.25$ (marked also in figs. 2 and 3 by vertical lines) with more details.

Figure 4 shows the cases studied. Apart from the time series plotted for each value of considered α we also plot the reconstructed phase portraits by using the delayed coordinate. The delay Δt has been chosen in the standard way using a quarter of excitation frequency. Note that for a harmonic oscillator such a deference is usually present between displacement and velocity. Interestingly the fractional derivatives introduces the change to this rule proportional to α

$$D^\alpha(\sin(x)) = \sin(x - \alpha\pi/2), \tag{7}$$

which could favour the bifurcations during changing α. In fig. 4 one can clearly identify the periodic solutions by looking for closed lines in the phase portrait (see figs. 4(b), (d)–(f)). However during the changes of α the system bifurcates from a period one solution (figs. 4(b) and (f)) to period four and period five solutions (see figs. 4(e) and (d), respectively). The other two cases shown in figs. 4(a) and (c) have a nonperiodic structure.

4 Fourier and multi-scale entropy analyses

To improve understanding of the behaviour of complex systems that manifest themselves in nonlinear behaviour, sample entropy analysis is becoming increasingly popular [30]. This method provides, for measured signals, a relative level
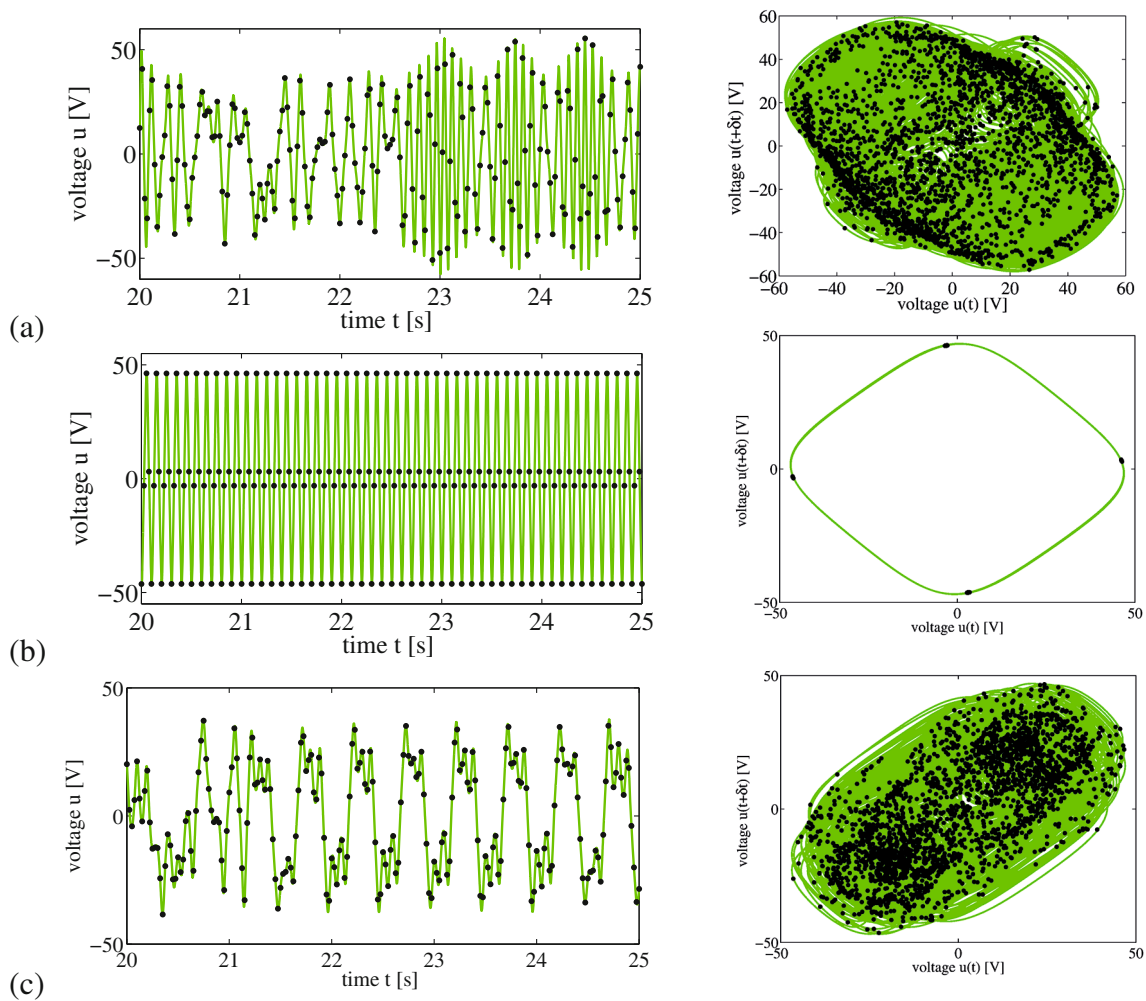
Fig. 4. Voltage open circuit time series and the corresponding phase portrait with delayed coordinate (the time delay Δt was fixed to one quarter of excitation period) for $\alpha = 0.35, 0.78, 0.85, 1.00, 1.195, 1.25$ for (a)–(f), respectively. The same α values were marked by vertical lines in figs. 2–3. The black stroboscopic points show the cycles of the voltage in terms of Δt (four points per excitation period).

of complexity of finite length time series. The concept of multi-scale entropy (MSE) is based on the coarse-graining procedure that uses a coarse-grained time series, as an average of the original data points within nonoverlapping windows by increasing the scale factor τ according to the following formula [31]:

$$u_j^{(\tau)} = \frac{1}{\tau} \sum_{i=(j-1)\tau+1}^{j\tau} u_i, \tag{8}$$

where $\mathbf{u}$ is a raw one-dimensional time series $\mathbf{u} = \{u_1, u_2, \ldots, u_N\}$.

MSE allows identification of dynamical system behaviour for variable scaling factor τ. It was also noted in [32] that the form/shape of the MSE is highly dependent on the time scales involved, and that the same MSE signatures can be found for dynamically very different systems.

Additionally, composite multi-scale entropy (CMSE) considers multiple choice of the nonoverlapping windows [33]. In this approach for each scale factor τ, the MSE calculation based on the time series of the coarse-grained $u_j^{(\tau)}$ (see fig. 5),

$$\mathrm{MSE}(\mathbf{u}, \tau, m, r) = \mathrm{SampEn}\left(\mathbf{u}^{(\tau)}, m, r\right). \tag{9}$$

where $m = 2$ is the pattern length and r is the similarity criterion and is usually chosen to be $r < \sigma_u$ [34]. Here σ_u is the standard deviation of the original time series and $u_i^{(1)} = u_i$.
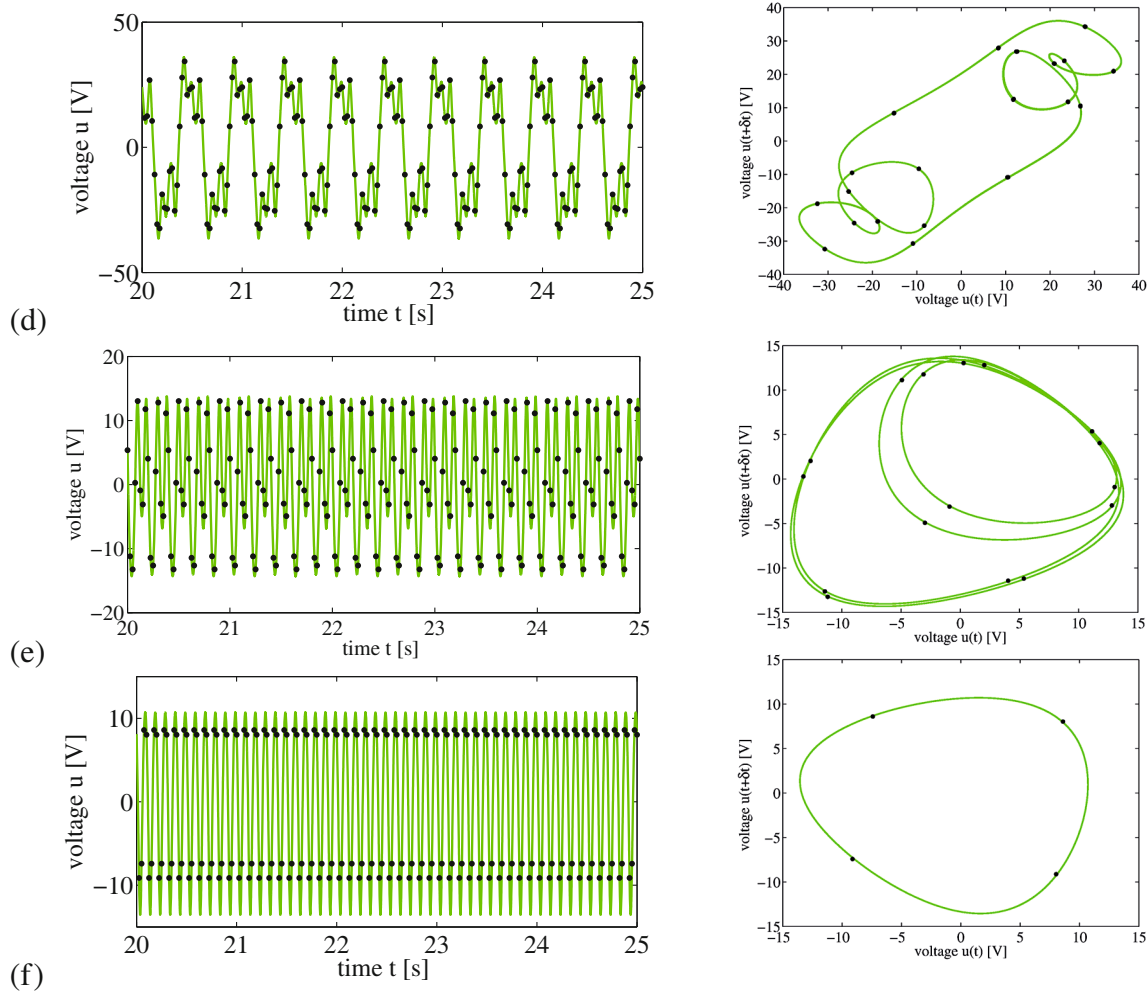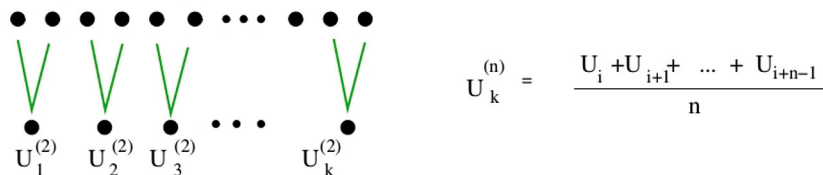
Fig. 4. Continued.

Fig. 5. Schematic picture showing the concept of higher scales.

To estimate $\mathrm{SampEn}(\mathbf{u}^{(\tau)}, m, r)$ we count the number of vector pairs denoted by $u^{(\tau)}(i)$ and $u^{(\tau)}(j)$ in the time series of length m and $m+1$ having distance $d[u^{(\tau)}(i), u^{(\tau)}(j)] < r$. We denote them by P_m and P_{m+1}, respectively. Finally, we define the sample entropy to be [35]

$$\mathrm{SampEn}\left(\mathbf{u}^{(\tau)}, m, r\right) = -\log \frac{P_{m+1}}{P_m}. \tag{10}$$

Strictly speaking, it is the minus of the logarithm of the conditional probability that two sequences with a tolerance r form points that remain within r of each other at the next point.

Continuing these research efforts Wu *et al.* [33] introduced the concept of a composite multi-scale entropy (CMSE), which for higher scale factor provides entropy more reliably than the usual multi-scale entropy by including multiple combinations of neighbour points. The prescribed algorithm for CMSE calculations is the following formula:

$$\mathrm{CMSE}(\mathbf{u}, \tau, m, r) = \frac{1}{\tau} \sum_{k=1}^{\tau} \mathrm{SampEn}\left(\mathbf{u}_k^{(\tau)}, m, r\right). \tag{11}$$
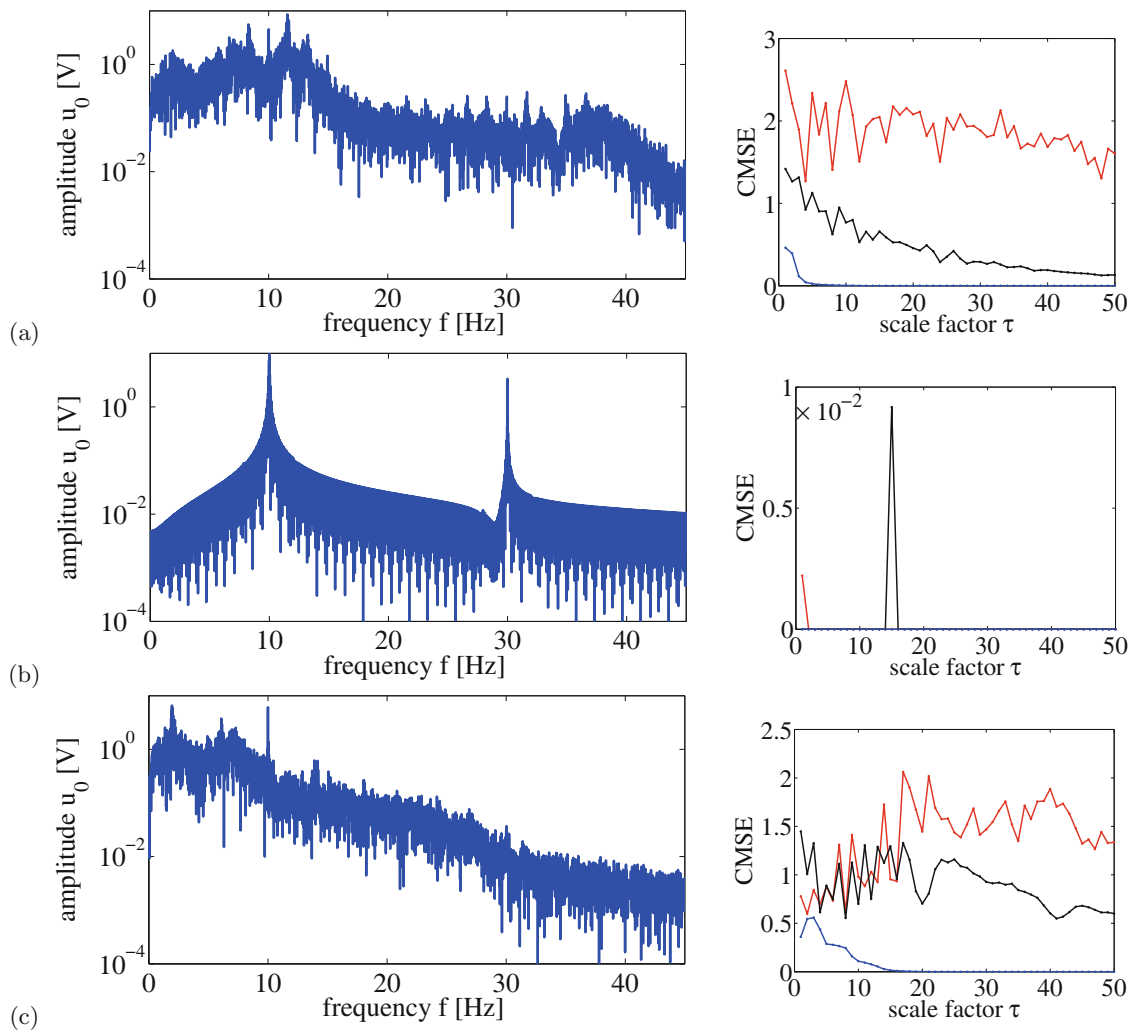
Fig. 6. Fourier spectra and CMSE for $\alpha = 0.35, 0.78, 0, 85, 1.00, 1.195, 1.25$ for (a)–(f), respectively. The same α values were marked by lines in figs. 2 and 3. The results of CMSE for $m = 2$ (length of the chain) and three values of the similarity factor r ($r = 0.01\sigma_u$ - red line, $0.1\sigma_u$ - black line, and $1\sigma_u$ - blue line). Note that oscillations of CMSE between large and nearly zero values or permanent zero value (for all lines) signal a regular solution. Otherwise the solution is chaotic (as in panels (a) and (c)). In fig. 6(f), where all CMSE (for $r/\sigma_u = 0.01, 0.1, 1$) collapsed to 0, there is additional $r = 2\sigma_u$ (green line).

The resulting Fourier spectra and CMSE are plotted in fig. 6 for the cases examined here. Note that the Fourier spectra are fairly broad for nonperiodic cases (see figs. 6(a) and (c)) and have discrete peak structures for the periodic cases (see figs. 6(b), (d)–(f)). Furthermore, because of nonlinearities, the peak structure appears in the multiples of excitation frequencies. On the other hand, the structures of multi-scale entropy plots are characterized by a permanent finite value of CMSE (especially in the red curve where the similarity factor takes the smallest value, $r = 0.01\sigma_u$) for a nonperiodic system responses. In contrast, for periodic solutions the entropy CMSE tends to 0. In this case the solution could oscillate with the change of scale (see figs. 6(b), (d)–(e)) or be permanently 0 (as in fig. 6(f)) for some coincidence in sampling and excitation frequencies. In the estimations of CMSE we used the series of the stroboscopic points plotted in fig. 4.

5 The 0-1 test

The "0-1 test", invented by Gottwald and Melbourne [36,37], can be applied for any systems of finite dimension to identify chaotic dynamics, however, it is based on the statistical properties of a single coordinate only. Thus it is suitable to quantify the response where only one parameter is measured in time. The test is related to the universal properties of dynamical systems, such as spectral measures, and can therefore distinguish a chaotic system from a regular one using a single variable.
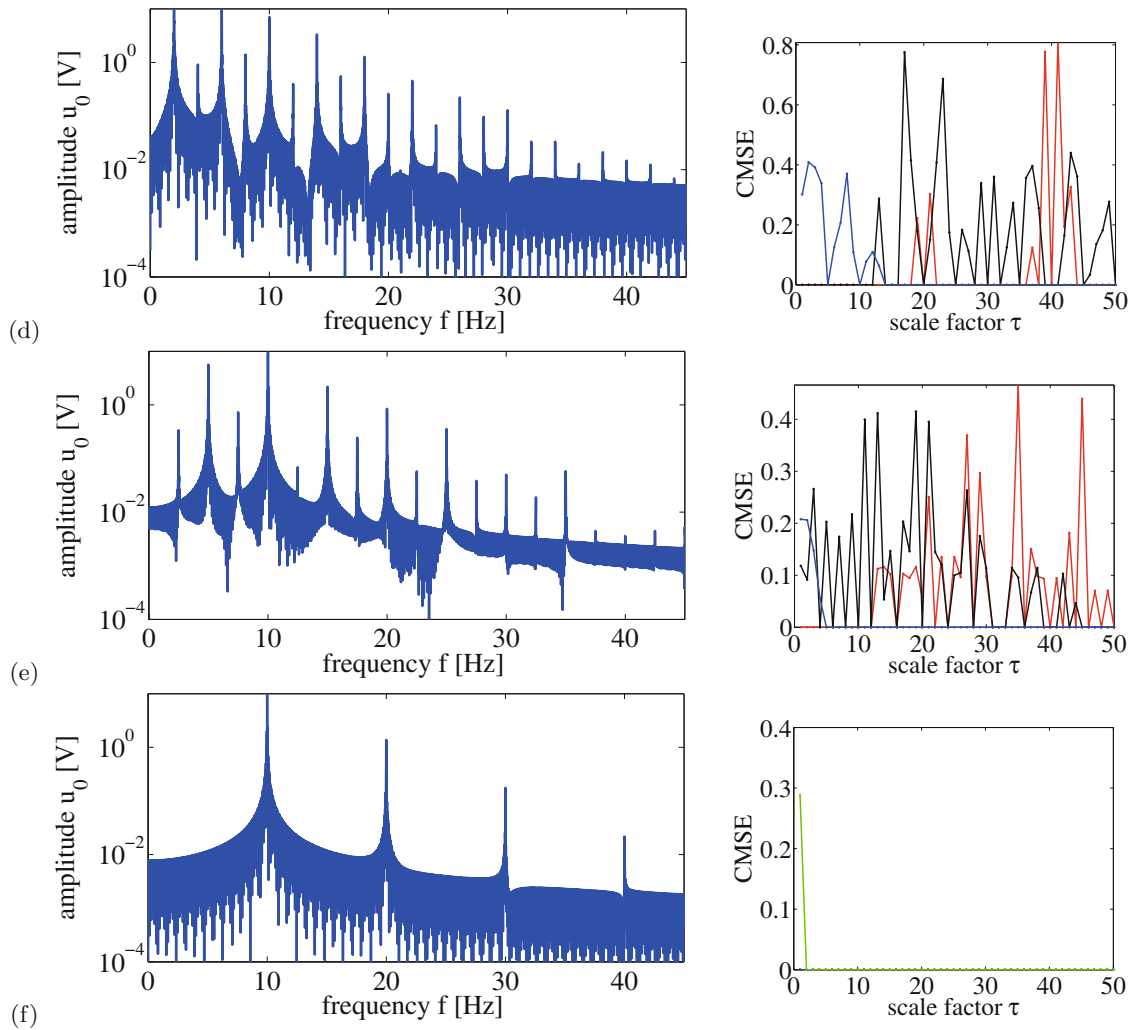
(d)

(e)

(f)

Fig. 6. Continued.

A particular advantage of the 0-1 test over the frequency spectrum is that it provides information regarding the dynamics in a single parameter value, similar to the Lyapunov exponent. However, the Lyapunov exponent can be difficult to estimate in any nonsmooth simulated system or measured data [38]. Therefore the 0-1 test can provide a suitable algorithm to identify the chaotic solution [39–44].

To start the analysis, we discretize the investigated time series $u(t) \rightarrow u(i)$ using the characteristic delay time Δt equal to one quarter of the excitation period $2\pi/\omega$ (as the points shown in figs. 3 and 4). This roughly indicates the vanishing of the mutual information [39,45]. Starting from one of the initial map coordinates $u(i)$, for sampling points $i = 1, \ldots, N$, we define new coordinates $p(n)$ and $q(n)$ as

$$p(n) = \sum_{j=0}^{n} \frac{(u(j) - \overline{u})}{\sigma_u} \cos(jc),$$

$$q(n) = \sum_{j=0}^{n} \frac{(u(j) - \overline{u})}{\sigma_u} \sin(jc), \tag{12}$$

where $n = 1, \ldots, N$, $\overline{u}$ denotes the average value of u, σ_u the corresponding standard deviation, and $c \in (0, \pi)$ is a constant. Note that $q(n)$ is a complementary coordinate in the two-dimensional space. Furthermore, starting from the bounded coordinate $u(i)$ we build a new series $p(n)$ which can be either bounded or unbounded depending on the dynamics of the examined process.

Continuing the calculation procedure, the total mean square displacement is defined as

$$M_c(n) = \lim_{N \to \infty} \frac{1}{N} \sum_{j=1}^{N} \left[(p(j+n) - p(j))^2 + (q(j+n) - q(j))^2 \right]. \tag{13}$$

The asymptotic growth of $M_c(n)$ can be easily characterised by the corresponding ratio $K_c'(n)$

$$K_c'(n) = \frac{\ln(M(n))}{\ln n}. \tag{14}$$

In the limit as $n \to \infty$ (in present calculations $n = n_{\max} = 270$, while $N = 2700$) we obtain the corresponding values of K_c for a chosen value of c. Note, our choice of the limits on $n_{\max}$ and N (in eqs. (13) and (14)) is consistent with that proposed by Gottwald and Melbourne [40,41,46]. $N, n_{\max} \to \infty$ but simultaneously $n_{\max}$ should be about $N/10$.

It is important to note that the parameter c acts like a frequency in a spectral calculation. If c is badly chosen, it could resonate with the excitation frequency or its super- or sub-harmonics. In the 0-1 test, a periodic motion would yield a regular behaviour in the (p,q)- plane with corresponding $M_c(n)$ constant in time. On the other hand, a nonperiodic motion is characterized by an expanding behaviour in the (p,q)-plane with corresponding $M_c(n)$ increasing in time [40]. The disadvantage of the test, its strong dependence on the chosen parameter c, can be overcome by a proposed modification. Gottwald and Melbourne [36,40] suggested randomly chosen values of c are taken and the median of the corresponding K_c-values are computed.

In [40] a covariance formulation is used with

$$K_c = \frac{\text{cov}(\mathbf{X}, \mathbf{M}_c)}{\sqrt{\text{var}(\mathbf{X})\text{var}(\mathbf{M}_c)}}, \tag{15}$$

where vectors $\mathbf{X} = [1, 2, \ldots, n_{\max}]$, and $\mathbf{M}_c = [M_c(1), M_c(2), \ldots, M_c(n_{\max})]$.

In the above, the covariance $\text{cov}(\mathbf{x}, \mathbf{y})$ and variance $\text{var}(\mathbf{x})$, for arbitrary vectors $\mathbf{x}$ and $\mathbf{y}$ of $n_{\max}$ elements, and the corresponding averages $\overline{x}$ and $\overline{y}$, respectively, are defined as

$$\text{cov}(\mathbf{x}, \mathbf{y}) = \frac{1}{n_{\max}} \sum_{n=1}^{n_{\max}} (x(n) - \overline{x})(y(n) - \overline{y}),$$
$$\text{var}(\mathbf{x}) = \text{cov}(\mathbf{x}, \mathbf{x}). \tag{16}$$

Note that using eqs. (15) and (16) automatically cancels out the means and eq. (12) can be defined without substraction of $\overline{u}$.

Finally, the median is taken of the K_c-values in eq. (15), corresponding to 100 equally spaced random values of $c \in (0, \pi)$. Such an average $\bar{K}$-value can now be estimated for various orders α. The differences between regular motion (circle like in the (p,q)-plane in figs. 7(b), (d)–(f)) and the chaotic one (random walking like in the (p,q)-plane in figs. 7(a) and (c)) are visible on figs. 7(a)–(f) plotted for $c = 1.0$. Apart from the pattern, it is also worth noticing the difference in scale, which is about ten times larger in figs. 7(a) and (c) as in figs. 7(a)–(f). The estimated values $\bar{K} = 0.993, -0.005, 0.994, 0.000, -0.005, -0.004$ for the cases (a)–(f) (see also figs. 2 and 3), respectively. This is the direct confirmation that the cases, in figs. 7(a) and (c), represent chaotic responses while the rest of cases, in figs. 7(b), (d)–(f), are related to various periodic responses.

6 Summary and conclusions

The occurrence of multiple relaxation times in visco-elastic materials is an important material property leading to hysteretic behaviour. Damping may be described by many ways, by introducing the extra degrees of freedom which could be related to the physical domains and/or to parametrize the hysteresis. We characterized the damping term by fractional derivative which uses memory as additional information of the actual state of the dynamical system. Its influence is reflected in the time delayed variables (in the Grunwald-Letnikov definition) or by the convolution with the fractional power function of time (in the Riemann-Liouville definition). In these treatments the weight coefficients of time delay importance are defined by a fractional power. In our case, the fractional derivative is based on the Tustin-Euler spectrum of frequencies related to the characteristic time delays.

By changing the fractional order in the damping term we study bifurcation between various periodic and chaotic vibrations. To examine the specific solutions we used the Fourier spectra and phase portraits. The results were quantified by multi-scale entropy through the 0-1 test. We noticed that a series of bifurcations were caused by the fractional derivative. For a large value of the fractional order alpha ($\alpha > 1$) the mechanical resonator is damped
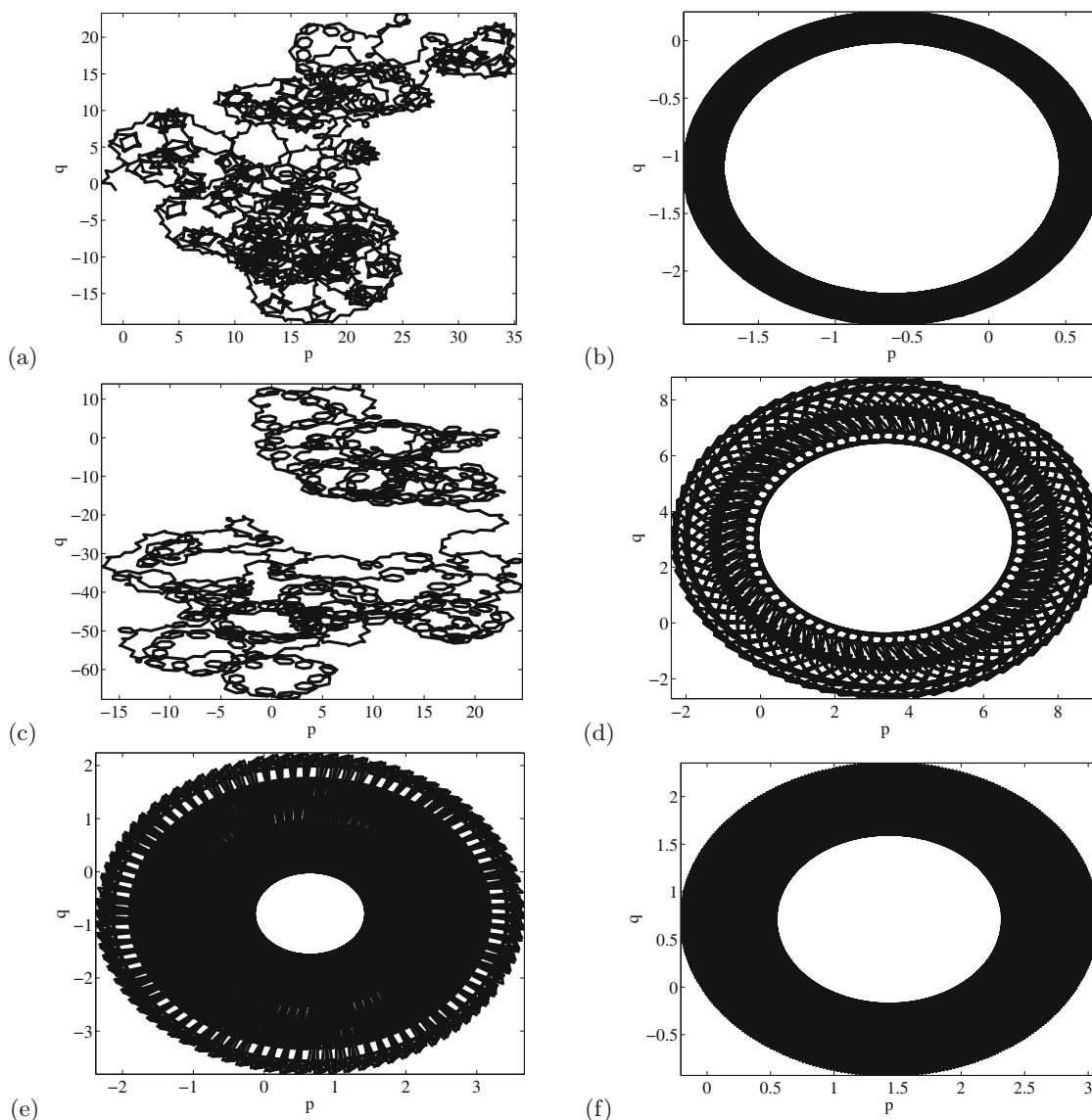
Fig. 7. Phase portraits in the space (p, q) $(p(n), q(n)$ for $n = 1, \ldots, 2700)$ for $c = 1$. The estimated 0-1 test parameters, $\bar{K}$, are $\bar{K} = 0.993, -0.005, 0.994, 0.000, -0.005, -0.004$ for fig. 7(a)–(f) (for the same α values as marked by vertical lines in figs. 2 and 3.) Note that the asymptotic value of the parameter $\bar{K} \to 0$ for regular motion and $\bar{K} \to 1$ for chaos (cases (a) and (c)).

strongly and its oscillations are limited to that of a single potential well. For small and medium values of alpha $(\alpha < 1)$ we noticed larger amplitude responses in both the mechanical resonator displacement and voltage output. However the power output significantly depended on the particular solution. For example, the appearance of chaotic vibrations reduced the harvested energy.

In most cases, nonlinear systems are characterised by multiple solutions including periodic and nonperiodic, and/or resonant and nonresonant solutions. By changing the systems parameters, the specific solutions undergo bifurcations leading to different power outputs. The results provided here regarding the system response will help designers of nonlinear energy harvesting devices by providing intuition when trying to optimise the power output.

References

1. H.A. Sodano, D.J. Inman, G. Park, Shock Vibr. Dig. **36**, 197 (2004).
2. E. Lefeuvre, A. Badel, A. Benayad, L. Lebrun, C. Richard, D. Guyomar, J. Phys. IV **128**, 177 (2005).
3. S.R. Anton, H.A. Sodano, Smart Mater. Struct. **16**, R1 (2007).
4. S.P. Beeby, M.J. Tudor, N.M. White, Meas. Scien. Technol. **17**, R175 (2006).
5. S.P. Pellegrini, N. Tolou, M. Schenk, J.L. Herder, J. Intell. Mater. Syst. Struct. **24**, 1303 (2012).
6. R.L. Harne, K.W. Wang, Smart Mater. Struct. **22**, 023001 (2013).
7. M.F. Daqaq, R. Masana, A. Erturk, D.D. Quinn, Appl. Mech. Rev. **66**, 040801 (2014).
8. F. Cottone, H. Vocca, L. Gammaitoni, Phys. Rev. Lett. **102**, 080601 (2009).
9. L. Gammaitoni, I. Neri, H. Vocca, Appl. Phys. Lett. **94**, 164102 (2009).
10. B.P. Mann, B.A. Owens, J. Sound Vibr. **329**, 1215 (2010).
11. R. Ramlan, M.J. Brennan, B.R. Mace, I. Kovacic, Nonlinear Dyn. **59**, 545 (2010).
12. M. Ferrari, V. Ferrari, M. Guizzetti, B. Ando, S. Baglio, C. Trigona, Sens. Actuators A: Phys. **162**, 425 (2010).
13. D.D. Quinn, A.L. Triplett, L.A. Bergman, A.F. Vakakis, J. Vibr. Acoust. **133**, 011001 (2011).
14. R. Masana, M.F. Daqaq, J. Sound Vibrat. **330**, 6036 (2011).
15. G. Sebald, H. Kuwano, D. Guyomar, B. Ducharne, Smart Mater. Struct. **20**, 102001 (2011).
16. A. Erturk, D.J. Inman, J. Sound Vibrat. **330**, 2339 (2011).
17. D.A.W. Barton, S.G. Burrow, L.R. Clare, J. Vibrat. Acoust. **132**, 021009 (2010).
18. G. Litak, M.I. Friswell, S. Adhikari, Appl. Phys. Lett. **96**, 214103 (2010).
19. S.F. Ali, S. Adhikari, M.I. Friswell, S. Narayanan, J. Appl. Phys. **109**, 074904 (2011).
20. C. McInnes, D. Gorman, M.P. Cartmell, J. Sound Vibrat. **318**, 655 (2008).
21. C.A.K. Kwuimy, G. Litak, M. Borowiec, C. Nataraj, Appl. Phys. Lett. **100**, 024103 (2012).
22. W. Martens, U. von Wagner, G. Litak, Eur. Phys. J. ST **222**, 1665 (2013).
23. J. Cao, S. Zhou, D.J. Inman, Y. Chen, Nonlinear Dyn. **80**, 1705 (2015).
24. C.A.K. Kwuimy, G. Litak, C. Nataraj, Nonlinear Dyn. **80**, 491 (2015).
25. A. Syta, C.R. Bowen, H.A. Kim, A. Rysak, G. Litak, Meccanica (2015), DOI: 10.1007/s11012-015-0140-1.
26. Y.Q. Chen, K.L. Moore, IEEE Trans. Circ. Syst. **49**, 363 (2002).
27. C. Ma, Y. Hori, Nonlinear Dyn. **38**, 171 (2004).
28. J.A.T. Machado, Commun. Nonlinear Sci. Numer. Simulat. **14**, 3492 (2009).
29. C. Onat, M. Sahin, Y. Yaman, Aircr. Eng. Aerosp. Technol. **84**, 203 (2012).
30. M. Borowiec, A. Rysak, D.H. Betts, C.R. Bowen, H.A. Kim, G. Litak, Eur. Phys. J. Plus **129**, 211 (2014).
31. M. Costa, A.L. Goldberger, C.-K. Peng, Phys. Rev. Lett. **89**, 68102 (2002).
32. R.A. Thuraisingham, G.A. Gottwald, Physica A **366**, 323 (2006).
33. S.-D. Wu, C.-W. Wu, S.-G. Lin, C.-C. Wang, K.-Y. Lee, Entropy **15**, 1069 (2013).
34. M. Costa, C.-K. Peng, A.L. Goldberger, J.M. Hausdorff, Physica A **330**, 53 (2003).
35. J.S. Richman, J.R. Moorman, Am. J. Physiol. **278**, H2039 (2000).
36. G.A. Gottwald, I. Melbourne, Proc. R. Soc. London A **460**, 603 (2004).
37. G.A. Gottwald, I. Melbourne, Physica D **212**, 100 (2005).
38. A. Wolf, J.B. Swift, H.L. Swinney, J.A. Vastano, Physica D **16**, 285 (1985).
39. G. Litak, A. Syta, M. Wiercigroch, Chaos Solitons Fractals **40**, 2095 (2009).
40. G.A. Gottwald, I. Melbourne, SIAM J. Appl. Dyn. Syst. **8**, 129 (2009).
41. G.A. Gottwald, I. Melbourne, Nonlinearity **22**, 1367 (2009).
42. G. Litak, S. Schubert, G. Radons, Nonlinear Dyn. **69**, 1255 (2012).
43. B. Krese, E. Govekar, Nonlinear Dyn. **67**, 2101 (2012).
44. G. Litak, D. Bernardini, A. Syta, G. Rega, A. Rysak, Eur. Phys. J. ST **222**, 1637 (2013).
45. H. Kantz, T. Schreiber, *Non-linear Time Series Analysis* (Cambridge University Press, Cambridge, 1977).
46. I. Melbourne, G.A. Gottwald, Nonlinearity **21**, 179 (2008).